Wind Energy

WIND ENERGY
Wind Energ. (2015)
Published online in Wiley Online Library (wileyonlinelibrary.com). DOI: 10.1002/we.1877

RESEARCH ARTICLE

Time-adaptive wind turbine model for an LES framework

V. Sharma[1], M. Calaf[2], M. Lehning[1] and M. B. Parlange[1,3]

[1] School of Architecture, Civil and Environmental Engineering, EPFL, Lausanne, Switzerland
[2] Department of Mechanical Engineering, University of Utah, USA
[3] Department of Civil Engineering, University of British Columbia, Vancouver, Canada

ABSTRACT

Most large-eddy simulation studies related to wind energy have been carried out either by using a fixed pressure gradient to ensure that mean wind direction is perpendicular to the wind turbine rotor disk or by forcing the flow with a geostrophic wind and timely readjusting the turbines' orientation. This has not allowed for the study of wind farm characteristics with a time-varying wind vector. In this paper, a new time-adaptive wind turbine model for the large-eddy simulation framework is introduced. The new algorithm enables the wind turbines to dynamically realign with the incoming wind vector and self-adjust the yaw orientation with the incoming wind vector similar to real wind turbines. The performance of the new model is tested first with a neutrally stratified atmospheric flow forced with a time-varying geostrophic wind vector. A posteriori, the new model is used to further explore the interaction between a synthetic time-changing thermal atmospheric boundary layer and an embedded wind farm. Results show that there is significant potential power to be harvested during the unstable time periods at the cost of designing wind turbines capable of adapting to the enhanced variance of these periods. Stable periods provide less power but are more constant over time with an enhanced lateral shear induced by an increased change in wind direction with height. Copyright © 2015 John Wiley & Sons, Ltd.

KEYWORDS
LES; wind energy; wind turbines

Correspondence
M. Calaf, Department of Mechanical Engineering, University of Utah, 50 S. Central Campus Dr., MEB 2110, Salt Lake City, Utah 84112, USA.
E-mail: marc.calaf@utah.edu

Received 29 April 2014; Revised 5 May 2015; Accepted 4 June 2015

1. INTRODUCTION

Studies in wind energy have developed rapidly over the past few years, with works investigating a wide range of problems, such as wind turbine aerodynamics,[1,2] wake interactions[3–5] or large-scale wind farm and atmosphere interaction.[6–9] The large-eddy simulation (LES) technique has increasingly been implemented to gain insight into the wind energy question. Its inherent high spatio-temporal resolution, together with its capacity for resolving the large-scale flow phenomena, has allowed for a wide variety of LES wind energy studies. In most works, the flow is forced with a pressure gradient to better control the mean wind direction of the turbulent flow. While this procedure is simple and has provided great insight into the study of wake structures, harvesting of wind power in large wind farms or farm layout effects, it is a limiting factor for more realistic scenarios. New generation atmospheric LES codes have been proven to accurately reproduce time-changing atmospheric flows when forced with close-to-realistic conditions, including Coriolis effects.[10] Yet, it has not been possible to study wind turbine characteristics under such changing conditions because of the limited flexibility of the wind turbine models used within the LES simulations. Current turbine models do not allow for automatic rotation and alignment of the turbines' nacelle with the changing wind conditions; hence, the current needs to properly prescribe the incoming flow such that it is perpendicular to the turbines' rotor disk. Porté-Agel *et al.*[11] investigated the effect of wind direction change and the wind farm layout on wake interaction. This work required a large set of numerical simulations, each one forced with a fixed pressure gradient corresponding to a new wind vector orientation. Some studies[12,13] have performed precursor stable atmospheric boundary layer (ABL) simulations to generate inflow velocity fields for separate wind turbine simulations

to study the effect of mean atmospheric forcings on wind turbine wakes. Recent studies such as Sescu and Meneveau[14] utilize a 'proportional-integral' control algorithm that artificially constrains the mean flow to be in the streamwise direction while maintaining statistical stationarity. Coupled mesoscale–microscale simulation methods are being explored for wind resource estimation and for guiding wind farm siting and operational decisions.[15] The increasingly popular Weather Research and Forecasting model (WRF-LES), technique especially useful for studying flows in complex terrain and non-idealized settings, is being adopted for wind energy research as well. Notable works include Mirocha *et al.*,[16,17] where nested LES simulations with wind turbines modelled using the generalized actuator disk model have been used to study the ABL–wind turbine (WT) interaction in realistic forcing conditions and compared with field and turbine data. At the other end of the research spectrum is the development of high-fidelity aero-elastic models such as the Fatigue, Aerodynamics, Structures, and Turbulence (FAST) code[18] at National Renewable Energy Laboratory (NREL), United States with additional capabilities for wind turbine control mechanisms such as yaw-correction and pitch control.[19] These models provide a very detailed description of real-world wind turbines but require high spatial and temporal resolution of the flow to compute the WT forces, power output and loads. Thus, to the best of our knowledge, such models have not been used to parameterize wind turbines in simulations of large wind farms embedded in a full ABL simulation.

Previous works also show an increasing interest in better understanding the changes induced by the interaction of turbine wakes with the underlying land surface—e.g. changes in evapotranspiration, land surface temperature and crop growth.[20–24] Assessing these changes experimentally would require large and expensive field experiments.[25,26] In addition, experimental conditions are sometimes so complex that fully decomposing the effects of the multiple elements in play becomes an almost impossible task. Numerical simulations are a valuable tool to independently assess the effects of turbines, and for these numerical simulations to reproduce more realistic conditions, the simulations need to partly capture the time evolution of the atmospheric flow. Thus, for studying the behaviour of wind turbines, their corresponding wakes, and the interaction with the surrounding flow and land surface, a time-adaptive wind turbine algorithm is needed. At present, wind turbines timely synchronize their aerodynamic profile and yaw alignment with the changing mean wind conditions according to pre-established power curves and configured operational schemes. The time-varying flow conditions are extracted using wind vanes and cup anemometers installed at the nacelle, and the wind turbine adjusts to pre-established configuration setups. It is well known that wind conditions under convective conditions are radically different than those encountered under stably stratified regimes. Wind direction changes happen regularly under convective regimes with elevated turbulent intensity periods, while under stably stratified periods, the flow tends to be less turbulent. In this work, a numerical algorithm that permits for the wind turbine to automatically readjust its yaw alignment with the local incoming wind conditions is presented. The wind turbine algorithm is equipped with a flexible time averaging function that allows to compute the averaged incoming wind vector and dynamically adjusts the turbine's yaw. At present, the incoming wind vector is measured at hub height as with traditional wind vanes and cup anemometers installed behind the rotor blades. The new algorithm uses the actuator disk model with additional rotation similar to that used in Wu *et al.*,[27] and an LES code based on pseudo-spectral numerics and dynamic sub-grid-scale model, similar to the one presented in past works,[10,11,20,28] is implemented. In Section 2, the LES code is presented in detail together with the sub-grid model and the boundary conditions. Section 3 introduces the new time-adaptive wind turbine algorithm, and Section 4 introduces the study cases considered. Sections 5 and 6 describe two specific examples in which the new algorithm has been applied. Results are presented with respect to power availability at different daytime periods with the corresponding properties associated to this available power.

2. THE LARGE-EDDY SIMULATION APPROACH

The numerical code solves for the non-dimensional, filtered Navier–Stokes equations for an incompressible flow in hydrostatic equilibrium, together with the continuity equation. The rotational form of the filtered Navier–Stokes equations is used in order to ensure conservation of mass and energy of the inertial terms.[29] The effect of temperature is introduced into the momentum equations using a thermal buoyancy term as a result of using the Boussinesq approximation. The full set of equations being solved is therefore

$$\frac{\partial \tilde{u}_i}{\partial x_i} = 0 \tag{1}$$

$$\frac{\partial \tilde{u}_i}{\partial t} + \tilde{u}_j \left(\frac{\partial \tilde{u}_i}{\partial x_j} - \frac{\partial \tilde{u}_j}{\partial x_i} \right) = -\frac{1}{\rho} \frac{\partial \tilde{p}}{\partial x_i} - \frac{\partial \tilde{\tau}_{ij}}{\partial x_j} + g \left(\frac{\tilde{\theta} - \hat{\tilde{\theta}}}{\hat{\tilde{\theta}}} \right) + f(\tilde{u}_2 - v_G)\delta_{i1} - f(\tilde{u}_1 - u_G)\delta_{i2} + f_i \tag{2}$$

$$\frac{\partial \tilde{\theta}}{\partial t} + \tilde{u}_j \frac{\partial \tilde{\theta}}{\partial x_j} = -\frac{\partial \pi_j}{\partial x_j} \tag{3}$$

where $\tilde{\theta}$ is the filtered potential temperature, $\tilde{u}_i$ represents the LES-filtered velocity component in the i direction (i = 1, 2, 3) and $\tilde{p}$ is the resolved dynamic pressure term formulated so as to satisfy the divergence-free condition. The

deviatoric part of the momentum sub-grid stress term $\tilde{\tau}_{ij}$ is modelled with the Lagrangian scale-dependent model from Bou-Zeid *et al.*,[28] and the corresponding sub-grid scalar flux of potential temperature is modelled using the adaptation of the Lagrangian scale-dependent model for scalars introduced in Calaf *et al.*[20] The f term represents the Coriolis factor, and u_G and v_G represent the streamwise and cross-streamwise components of the geostrophic wind. Here, the tilde ($\tilde{}$) represents the LES filtering at the grid size (Δ), and ($\hat{}$) represents a secondary filtering operation at a spacing two times the grid size (2Δ). In Equation 2, δ_{ij} is the Kronecker delta ($\delta_{ij} = 1$ for $i = j$, 0 otherwise). The effect of atmospheric stratification is introduced by the potential temperature acting as an active scalar to modify the buoyancy of the air enhancing vertical displacements of air parcels and thus the momentum equation. This is introduced in Equation 2 using the Boussinesq approximation for the potential temperature. The effect of the wind turbines is introduced by a combination of a drag force and a tangential force, both acting into the momentum equation through the f_i term (see Section 3 for extended details). Because the simulations are carried out for large Reynolds numbers and the bottom surface and the wind turbines are parameterized, the viscous effects and the molecular diffusive effects are neglected. The numerical discretization of the equations follows the one introduced by Moeng[30] and Albertson *et al.*[31,32] This means that a pseudo-spectral discretization is used, with second-order finite differences in the vertical direction and Fourier transforms in the horizontal directions. Because of the Fourier-based methods in both horizontal directions, the domain is fully periodic and no lateral boundary conditions are needed: hence, the domain size tends to infinity in practical effects. A second-order Adams–Bashforth scheme is used for the time integration. In addition, the non-linear convective terms are dealized with the 3/2 rule.[33] The code is fully parallelized using Message Passing Interface, and the Fastest Fourier Transform in the West library[34] is employed for the Fourier transforms. The pressure solver for parallel runs is based on the pipeline Thomas algorithm.[35] As top boundary conditions, vertical velocity and gradients of velocity and temperature are set to zero. For the surface boundary conditions, a non-slip condition is imposed for the vertical velocity, and for the horizontal components of the momentum equation, an equivalent shear stress is imposed using the log-law with atmospheric stability correction,[28,36,37]

$$\tau_{i,3}(x,y,z_1) = -\left[\frac{k\sqrt{\left(\hat{\tilde{u}}_1^2 + \hat{\tilde{u}}_2^2\right)}}{ln\,(z_1/z_0) + \psi_m(z_1/L)}\right]^2 n_i \tag{4}$$

Here, i is the specific direction in the plane parallel to the surface ($i = 1, 2$) and n_i is a unitary directional vector defined as $n_i = \hat{\tilde{u}}_i/\sqrt{\hat{\tilde{u}}_1^2 + \hat{\tilde{u}}_2^2}$. The shear stress is imposed at $z_1 = \Delta z/2$ because of the staggered grid; thus, the velocities used are evaluated at that same height (first numerical grid point with values of $u_i, i = 1, 2$ available). The $\hat{\tilde{u}}_i$ represents a double filtering operation (at 2Δ grid spacing) on horizontal components of the flow, which is equivalent to a local average (see[28,37] for further details in this filtering). The surface roughness is constant over the entire numerical domain and has a value of $z_0 = 0.1$ m that corresponds to a ground surface with low crops.[38] For the numerical integration of the momentum equation, the vertical derivatives of the horizontal velocity components are also needed. These are parameterized at the first grid point also using Monin–Obukhov similarity theory,[39]

$$\partial_3 \tilde{u}_i(x,y,z_1) = \left(\frac{\sqrt{\tau}}{\kappa z}\right) n_i \tag{5}$$

with $\tau = \sqrt{\tau_{1,3}^2 + \tau_{2,3}^2}$. In a similar fashion as for the momentum, the kinematic sensible heat flux is computed at the first staggered grid point using Monin–Obukhov similarity theory,

$$H_s(x,y,z_1) = \frac{\kappa^2[\theta_s - \tilde{\theta}(x,y,z_1)]\left(\sqrt{\hat{\tilde{u}}_1^2 + \hat{\tilde{u}}_2^2}\right)}{\left[ln\left(\frac{z_1}{z_0}\right) + \psi_m(z/L)\right]\left[ln\left(\frac{z_1}{z_{0,h}}\right) + \psi_h(z/L)\right]} \tag{6}$$

where the surface temperature (θ_s) is imposed as bottom boundary condition for (see Section 4 for the specific values used). The stability correction functions (ψ) implemented are those from Brutsaert.[40] Different formulations exist depending upon stability, and the appropriate choice of functions is made based upon the Obukhov length (L), which is defined as

$$L = \frac{-u_\star^3\ \overline{\theta}_s}{\kappa\ g\ \overline{w'\theta'}_s} \tag{7}$$

where $u_\star$ is the friction velocity, $\overline{\theta}$ the mean potential temperature, κ de von Karman constant ($\kappa = 0.4$) and $\overline{w'\theta'}$ the surface sensible heat flux. For the unstable scenario, the stability correction functions are given by

$$\psi_m(z/L) = \begin{cases} ln(a - z/L) - 3b(z/L)^{1/3} + \frac{ba^{1/3}}{2} ln\left[\frac{(1+x)^2}{(1-x+x^2)}\right] + \\ \sqrt{3}ba^{1/3} tan^{-1}\left[(2x-1)/\sqrt{3}\right] + \psi_0 & \text{for } z/L \leq b^{-3} \\ \psi_m(b^{-3}) & \text{for } z/L > b^{-3} \end{cases} \tag{8}$$

and

$$\psi_h = [(1-d)/n] ln[(c + y^n)/c] \tag{9}$$

In the previous equation, $a = 0.33, b = 0.41, c = 0.33, d = 0.057, n = 0.78$ and $x = (-z/La)^{1/3}$. $\psi_0 = (-lna + \sqrt{3}ba^{1/3}\pi/6)$. For the stable scenario, the stability correction functions are

$$\begin{aligned} \psi_m(z/L) &= -a\, ln\Big[z/L + (1 + (z/L)^b)^{1/b}\Big] \\ \psi_h(z/L) &= -c\, ln\Big[z/L + (1 + (z/L)^d)^{1/d}\Big] \end{aligned} \tag{10}$$

where $a = 6.1, b = 2.5, c = 5.3$ and $d = 1.1$. The scalar surface roughness has been taken to be one-tenth of the momentum surface roughness ($z_{0,h} = z_0/10$).[41] The stability correction functions were initially developed from experimental studies on statistically homogeneous surfaces. It is understood that the wind turbines might have an effect on the precise parameterization of the stability correction functions, but lack of new experimental data on this precise matter does not allow for a better numerical approach at the present time.

3. THE TIME-ADAPTIVE WIND TURBINE ALGORITHM

Wind turbines are introduced as an additional body force in the Navier–Stokes equations similar to previous studies.[23,27,42–44] The force exerted by the turbine onto the fluid is computed using the classical actuator disk (AD) concept,[2] which states that a wind turbine induces an equivalent drag force proportional to the square of the unperturbed incoming wind velocity (u_∞^2), the frontal area swept by the rotor blades A and the thrust coefficient (C_T)

$$F_t = -\frac{1}{2}\rho C_T u_\infty^2 A. \tag{11}$$

The total area swept by the blades is treated as a circular disk as illustrated in 1(a). In a large wind farm with many turbines where the corresponding wakes interact with each other, it is not possible to define an unperturbed incoming velocity (u_∞). Instead, a local velocity in front of the turbine's rotor disk (u_d) is used. This is related to the upstream unperturbed velocity through the induction factor (a) as $u_\infty = u_d/(1-a)$.

The AD model is as a first-order approach to parameterizing wind turbines in LES, which does not capture blade-scale fluid motions such as tip vortices. However, a detailed numerical study from Wu *et al.*[27] showed that the AD model is sufficient to reproduce the far wake characteristics. By introducing additional tangential forces, the near wake characteristics can also be well reproduced without the need of numerically resolving the wind turbine blades. The model used in the present study is adopted from Meyers *et al.*,[45] which is similar to the AD with rotation model proposed by Wu *et al.*,[27] but with further simplifications regarding geometry and operation of the wind turbine blades. The forces are introduced by the model as described as follows:

$$\begin{aligned} f_t &= -\frac{1}{2}\rho C_T' \langle\overline{u}\rangle_d^2 \\ f_\theta &= \frac{1}{2}\rho C_P' \langle\overline{u}\rangle_d^2 \frac{\langle u\rangle_d}{\Omega r} \end{aligned} \tag{12}$$

where f_t is the standard drag force per unit area and f_θ is the tangential force per unit area at distance r from the centre. The actual force can be found by multiplying Equation (12) with an area element $rdrd\theta$. These parameterizations use 'modified' thrust and power coefficients, C_T' and C_P', respectively. To avoid the local heterogeneities in the velocity field and because the turbine disk is composed of many LES grid points, a disk-averaged velocity is used to compute the thrust on the flow

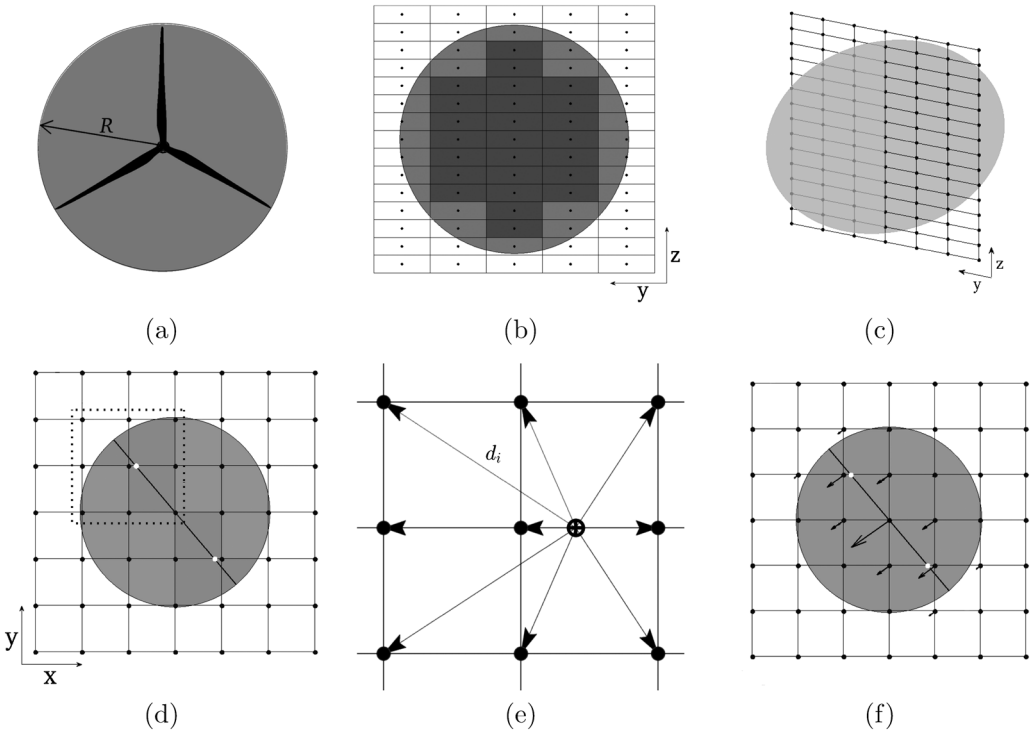

Figure 1. Computational details of the new wind turbine algorithm. Subplot (a) shows a scheme of the classic actuator disk, and subplot (b) shows the numerical decomposition of the actuator disk on a regular LES grid. The cells near the boundary of the disk (e.g. light grey coloured cells) have area overlap coefficient $(\gamma_{i,j}) < 1.0$. Inner cells (e.g. cells coloured dark grey) have $\gamma_{i,j} = 1.0$. Subplot (c) illustrates the misalignment of a wind turbine with respect to the LES grid, because of the changing incoming wind conditions. Subplot (d) is a top view of the wind turbine rotor disk (solid black line), the surrounding LES grid points (coloured black) and 'pseudo-LES' grid points (coloured white). Subplot (e) illustrates the 'pseudo-LES' grid point $(\oplus)$ and the closest LES grid points $(\bullet)$. Subplot (f) illustrates the final distribution of forces because of a misaligned wind turbine.

because of the spinning blades. Additionally, the disk-averaged velocity is averaged in time using an exponential weighted moving average to secure the numerical stability of the LES code by avoiding shocks and discontinuities. In Equation (12), $\langle\ \rangle_d$ represents disk averaging, and the overline ($\bar{}$) represents time averaging.

For the complete derivation of the previous expressions, the reader may refer to Meyers and Meneveau.[45] Only a brief summary of the assumptions used to derive Equation (12) is provided here for the sake of brevity. The derivation begins using the blade element-momentum theory, which combines the concept of conservation of linear and angular momentum with the blade element forces. This is based on the premise that these forces are solely responsible for the change in momentum of air passing through an annular disk.[2] It is assumed that the blades are 'optimally adapted' to the time-averaged incoming velocity ($\overline{V}$) such that the tip–speed ratio ($\lambda = \omega R/\overline{V}$) remains constant. It is also assumed that the ratio of lift and drag coefficients of the blades is kept constant using active pitch control. These optimality conditions imply that a detailed description of the blade geometry is no longer necessary. Balancing the lift and drag forces with the change in momentum and recasting the resulting equations in standard expressions for thrust and drag forces result in new coefficients C'_P and C'_T. These are related to standard coefficients as $C'_P = C_P/(1-a)^3$ and $C'_T = C_T/(1-a)^2$, respectively. In this work, values for C'_P, C'_T and a are chosen as 0.8, 1.334 and 0.25, respectively. Angular velocity (Ω) is fixed at 1.5 rad s^{-1} or 3.33×10^3 dimensionless units. These values are similar to the values in Meyers and Meneveau.[45]

Numerical implementation of the wind turbine model requires that the local forces described in Equation 12 are distributed onto the LES grid points. In this context, two mutually exclusive and exhaustive scenarios arise based on the orientation of the disk with respect to the LES mesh—the 'perfectly aligned' case where the WT disk is coplanar with one of the two vertical cartesian coordinate surfaces and the more general 'misaligned' case. Before these cases are analysed, consider (x, y, z) to be the streamwise, cross-stream and vertical directions respectively of the LES mesh. Figure 1(b) presents an example of the 'perfectly aligned' case where the WT is aligned with the y–z plane. The points represent the LES grid points, and the associated 'cell' for each point is created by a mesh with spacing of Δy and Δz in the horizontal and vertical directions, respectively. Local forces are computed using Equation (12) on a fine, disk-attached, cartesian 1000×1000 mesh with a resolution of 0.1 m. These forces are then 'upscaled' to LES grid points by a filtering operation.

The upscaled normal and tangential forces (F_t and F_θ, respectively) at any LES grid point $(y,z) \equiv (i,j)$ in Figure 1(b) can be computed as

$$\begin{aligned} F_t^{(i,j)} &= \frac{1}{\rho(\Delta x \Delta y \Delta z)} \iint f_t \, ker(y',z') \mathrm{d}y' \mathrm{d}z' \\ F_\theta^{(i,j)} &= \frac{1}{\rho(\Delta x \Delta y \Delta z)} \iint f_\theta \, ker(y',z') \mathrm{d}y' \mathrm{d}z' \end{aligned} \tag{13}$$

where $ker(y,z)$ is the kernel of the filter used for upscaling. In this work, the filter has a kernel, $ker_{i,j}(y',z') = BOX(y') \times BOX(z') \times H(R - \|(y',z')\|)$, where

$$BOX(y') = \begin{cases} 1 & j - \frac{\Delta y}{2} \le y' \le j + \frac{\Delta y}{2} \\ 0 & \text{elsewhere} \end{cases} \tag{14}$$

with analogous formulation for $BOX(z')$. The Heaviside function (H) is used to restrict the upscaling operation to within the WT disk. This kernel implies that all local forces within a cell are upscaled to its associated LES grid point. A common kernel used in other studies is the Gaussian kernel.[27,46,47] The Gaussian filter however requires a width parameter as input. Additionally, it is not conservative when applied numerically. Note that the upscaled forces are normalized by density (ρ) and volume ($\Delta x \Delta y \Delta z$) such that they can be directly added to the filtered LES equations that are solved per unit mass. The integration is computed numerically on the fine mesh. Because the local drag force term (f_t) is equal throughout the disk, the expression for the upscaled drag force (F_t) can be reduced to

$$F_t^{(i,j)} = -\frac{1}{2} C_T' \langle \overline{u} \rangle_d^2 \frac{\gamma_{i,j}}{\Delta x} \tag{15}$$

where overlap coefficient $\gamma_{i,j}$ is the fraction of area of the cell associated to point (i,j) that lies within the disk. In Figure 1(b), for example, the interior cells with dark shading have $\gamma_{i,j} = 1$. For the boundary cells $\gamma_{i,j} < 1$, the precise value can be computed by using the relationship $\iint ker_{i,j}(y',z') \mathrm{d}y' \mathrm{d}z' = \gamma_{i,j} \Delta y \Delta z$.

It is clear that the 'perfectly aligned' case is an idealized scenario. Indeed, the majority of previous works used a mean pressure gradient in the streamwise direction to enforce the mean flow direction in order to model the WTs as being perfectly aligned. In this study, a new WT model is developed that allows treatment of non-idealized cases of misaligned WTs with respect to the cartesian LES grid. This is needed to study the interaction of WTs with time-changing ABL conditions. A novel methodology to suitably model the generic 'misaligned' scenario is described as follows. Figure 1(c) shows a WT disk 'out of plane' of the y–z coordinate surface unlike Figure 1(b). The essential problem with the 'misaligned' scenario is that in most cases, the LES grid points lying along the vertical diameter are the only LES points on the disk. This is better illustrated by looking at a horizontal plane cutting through the WT disk at hub height, as shown in Figure 1(d). In this figure, the shaded circular region marks the horizontal extent of the WT disk in all possible orientations. The inclined black line corresponds to the projection of the disk in the orientation shown in Figure 1(c). Here, the cartesian grid represents the LES grid lines. It can be seen that, besides the center point, there are no other LES grid points within the disk. To solve this problem, a two-step process is followed. First, local forces are computed using the disk-attached fine mesh and upscaled to 'pseudo-LES' grid points as it was carried out in the 'perfectly aligned' case. The 'pseudo-LES' grid points are identified as follows. Consider the normal to the WT disk to be oriented along the direction of the incoming horizontal velocity. Let the angle made by the normal with the x-axis be denoted by ξ. If $\xi < 45°$, LES grid lines parallel to x-axis are chosen, else those parallel to y-axis are chosen. The corresponding intersection of the chosen grid lines with the WT disk is identified as 'pseudo-LES' grid points. As an illustration, in Figure 1(d), ξ is slightly less than 45°. Thus, grid lines parallel to x-axis are chosen, and their intersection with the disk is considered as the 'pseudo-LES' grid points (shown in Figure 1(d) and (f) as white grid points). The next step involves distributing the upscaled forces from the 'pseudo-LES' points to the nearest LES grid points in the same horizontal plane using the inverse distance weighting technique.[48] In Figure 1(d), a region surrounding one of the pseudo-LES grid points is demarcated by a dotted square. This region is zoomed into in Figure 1(e), which shows a nine-point stencil of LES grid points (•) containing a single 'pseudo-LES' grid point (⊕). Let the upscaled force at this point be $F_\oplus$. Then the resulting force at the ith LES grid point F_i is computed as follows:

$$F_i = F_\oplus \frac{d_i^{-1}}{\sum_i d_i^{-1}} \tag{16}$$

where d_i is the distance between the 'pseudo-LES' grid point and the ith LES grid point. An example of the resulting force field in a 'misaligned' scenario is presented in Figure 1(f). The arrows are scaled according to magnitude of force. Tangential forces have been neglected for the sake of clarity, and hence, all force lines are normal to plane of the WT. The error induced in the previous approximation is that the forces are no longer originating at the same plane but are distributed in a 3D 'cloud' of LES grid points surrounding the 'misaligned' WT disk. To summarize the parameterizations in the two

scenarios, in the 'perfectly aligned' case, local forces from Equation 12 are upscaled directly to the LES grid points using Equation (13), whereas in the 'misaligned' scenario, the local forces are first upscaled to the 'pseudo-LES' grid points, which are further distributed onto the LES grid points using inverse distance weighting. (Note that in the very exceptional case of $\xi = 45°$, the 'pseudo-LES' grid points coincide with the LES grid points.)

4. STUDY CASES

A standard simulation under neutral atmospheric conditions is developed to test the performance of the new wind turbine model (A), and a *synthetic* diurnal cycle (B) is used to explore the changes occurring within a large wind farm because of thermal variations in the flow. Simulations are performed in a computational domain of size $(\pi \times \pi \times 2)z_i$, where z_i is the height of the initial boundary layer, set at 1000 m. The numerical domain is decomposed in $N_x = N_y = 128$ and $N_z = 256$ grid points in the corresponding Cartesian directions. The time step for the simulations is fixed to 0.2 s physical time, or equivalently 1.2×10^{-3} of non-dimensional time units (time is normalized with u_G and z_i).

Initially, a *warm-up* simulation was run to obtain fully developed velocity and scalar fields, which were a posteriori used to initialize the two performance tests. The *warm-up* simulation was developed by considering a neutrally stratified ABL with an imposed constant surface temperature of 290 K. The ABL was forced using a constant geostrophic wind $(u_G, v_G) \equiv (6, 0)$ m s^{-1}. The potential temperature was initialized with a constant value of 290 K until z_i (ensuring the neutral stratification also close to the surface), along with a capping inversion of 0.012 K m^{-1} from z_i to the top of the domain. For the top boundary, the temperature gradient was set to zero. The implemented wind turbines had a hub height (z_h) of 100 m, with a diameter (D) fixed at 100 m. A total of 24 wind turbines were placed in a rectilinear grid pattern, with four rows and six columns, such that the spacing in the x and y directions is 8 D and 5 D, respectively. Note that the LES code uses periodic boundary conditions; thus, the wind farm is essentially infinite. The *warm-up* simulation was run for 17 h of physical time (367.2 units of non-dimensional time) such that the flow is fully developed and a wind turbine array boundary layer is established. The velocity and scalar fields at the end of this simulation were stored and reused as initial conditions for the following two study cases (A and B).

With the aim of testing the performance of the new wind turbine algorithm, the *warm-up* simulation was continued for an extra 18 h. During the initial 6 h of physical time, the geostrophic wind was progressively rotated up to 30° around the vertical axis. Next, the simulation was continued for an additional 12 h after the rotation was completed, until a new equilibrium was established. The absolute magnitude of the geostrophic wind vector was kept constant during the course of the simulation. The wind turbines progressively corrected their yaw orientation every 10 min based on the time-averaged orientation of the velocity at the turbine rotor disk. For this specific study case, the time averaging was carried out over a time period of 10 min; however, this is an adjustable variable. Results will show how the wind turbines' yaw orientation progressively follows the mean incoming wind.

The second study case consists of a *synthetic* ABL diurnal cycle also with wind turbines. To simulate the diurnal cycle, a sinusoidal function with a 24 h time period and an amplitude of 8.7 K (which is 3% of the fixed surface temperature of 290 K) was imposed as a time-varying surface boundary condition. Figure 3(a) shows the change in surface temperature, $\Delta\theta$ ($\Delta\theta = \theta_s(t) - \theta_s(t_0)$ with $\theta_s(t_0) = 290$ K). The simulation was run for 50 h of physical time, executing two complete diurnal cycles within that time period. The computational time for such simulations was 3600 and 10,000 CPU hours for study cases A and B, respectively. The simulations exhibit some of the main characteristics of the flow in a large wind farm under a highly temporally and spatially variable atmospheric flow. This analysis has only been possible thanks to the flexibility of the new numerical algorithm that permits the wind turbines to dynamically adapt to the changing surrounding conditions.

5. STUDY CASE (A): IMPOSED TIME-VARYING GEOSTROPHIC WIND UNDER A NEUTRAL ATMOSPHERIC STRATIFICATION

The aim of the first study case is to check whether the new wind turbine model is able to adapt to the time-changing incoming wind vector. Towards this aim, the mean flow of the ABL was progressively rotated in time, by linearly rotating the geostrophic wind. For the sake of simplicity and to be able to only focus on the performance of the wind turbines in readjusting to an ABL with rotating mean flow, an atmospheric neutral stratification was considered.

The simulation was initialized with the velocity and scalar fields from the *warm-up* simulation (see Section 4 for further details). Initially, the wind turbines had a mean orientation of 25°. The geostrophic wind was made to rotate by an additional 30° in the following 6 h, and later, it was kept fixed for the final 12 h. The wind turbines' configuration is set up such that wind turbines correct their orientation every 10 min, based on the time-averaged orientation of the rotor disk-averaged velocity $(\overline{\tan^{-1}(\langle v\rangle_d/\langle u\rangle_d)})$.

Figure 2 shows the change in orientation of the mean flow at hub height, with respect to the streamwise direction (x) (represented by the dashed line), together with the time adapting orientation of the wind turbines (solid line). The turbines' orientation has been averaged over the 24 WTs, and the shaded region presents the corresponding standard deviation between the different wind turbines in the farm. The *staircase* shape of the turbine's curve is due to the 10 min averaging step.

Results show how the WTs are capable of tracking the changing mean flow direction and correcting their own orientation accordingly. Note that the mean flow at the hub region experiences inertia to rotation. Thus, the rotation is slower than the rotation of the forcing geostrophic wind. The simulation should be rotationally invariant, which means that in the limiting case of a fully developed flow with the rotated geostrophic wind, results should be statistically similar to the *warm-up* simulation. However, the limiting case is approached through oscillations in velocity magnitude and orientation. In Figure 2, the orientation of the mean flow initially overshoots the theoretically enforced flow orientation, reaching a maximum orientation of 65°, opposed to the 55° expected. However, by the end of the simulation, the flow recovers from its own inertia and becomes consistent with the enforced orientation with the flow as well as wind turbines having orientation of 55°. The flow inertia, in terms of magnitude, can be observed in Figure 3(a), where the magnitude of the horizontal velocity at hub height decelerates in the first 6 h, coinciding with the period of rotation of the geostrophic wind. Once the enforced rotation stops, the simulation proceeds towards the new equilibrium stage, which under rotational invariance

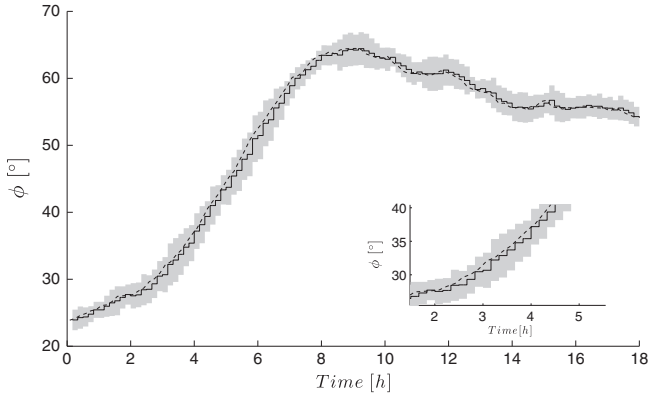

Figure 2. Time-changing mean horizontal wind orientation at hub height (dashed line) and time readjustment of the wind turbine's averaged yaw (solid line). The grey shaded region represents the standard deviation of the yaw orientation between the different wind turbines. The run time for this test is 18 h, where the geostrophic wind is constantly rotated over the first 6 h and kept fixed for the following 12 h.

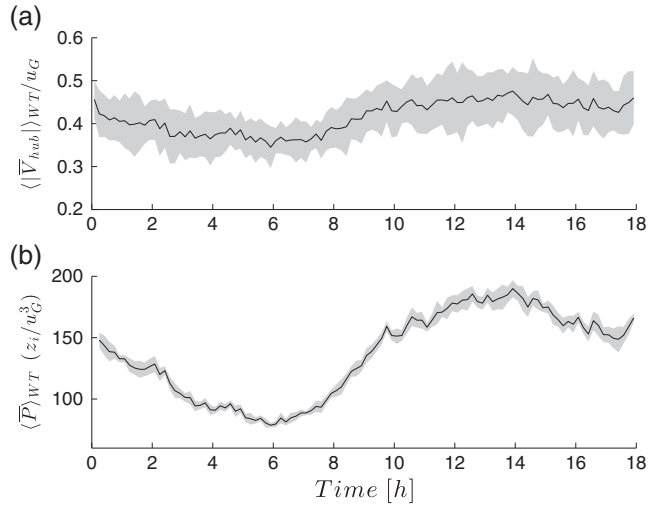

Figure 3. Time evolution of magnitude of mean velocity at hub height (a) and the extracted power (b). The shaded grey area represents the corresponding standard deviation of the mean wind velocity and extracted power between the 24 wind turbines.

should bear statistical similarity to the conditions at the start of simulation (A). It can be seen that horizontal velocity at the hub indeed accelerates to finally reach a similar value by the end of the simulation (at 18 h) to the one from the beginning.

The power extracted from the ABL by the WTs can be computed by considering all the points in the domain that are imparted volume forces arising because of the wind turbines and the velocities at those corresponding points. Thus, for any wind turbine i, the power available is computed as follows:

$$P_i = \sum_j \vec{F}_{i,j} \cdot \vec{u}_{i,j} \tag{17}$$

where the summation index runs over all the LES points imparted with force due to the ith WT. Initially, the corresponding WTs power is time averaged every 10 min ($\overline{P_i}$), and a posteriori, averaging is also carried out over all the WTs ($\langle \overline{P} \rangle_{WT}$). Note that the power computed using Equation (17) is not the power extracted by the rotor, and to be converted to electricity, but reflects the mean kinetic energy lost from the ABL because of the presence of wind turbines. In Figure 3(a), the normalized mean velocity at hub height and its standard deviation are presented. The resultant wind farm averaged power, together with the corresponding standard deviation, is shown in Figure 3(b). Note that the mean averaged velocity is non-dimensionalized with the geostrophic wind and the wind farm averaged power with the boundary layer height and the geostrophic wind as well. Following the same trend as the mean velocity, the power decreases up to the 6 h threshold, on account of decreasing hub velocity, and then increases between 6 and 14 h, after which it decreases again at the end of the simulation, at 18 h.

6. STUDY CASE (B): A DIURNAL CYCLE

In the previous section, it has been shown that the new numerical algorithm performs well for modelling time-adaptive wind turbines, with the wind turbines adjusting to the time-varying wind vector. Therefore, the new wind turbine algorithm allows for the modelling of wind turbines within a realistic time-varying diurnal cycle flow, where the wind conditions dramatically change with the change in atmospheric stratification. Taking advantage of this new flexibility, a synthetic diurnal cycle is used to begin exploring in a first-order approximation, the interaction between a large wind farm and a characteristic thermal ABL. To simulate a synthetic diurnal cycle, a time-varying boundary condition for the surface temperature was enforced. For ease of analysis, a sinusoidal function with a time period of 24 h of physical time and an amplitude of 8.7 K (which is 3% of the fixed surface temperature of 290 K) was imposed as shown in Figure 4(a). The additional simulation parameters were kept equal to the *warm-up* simulation, from which the present study case was initialized.

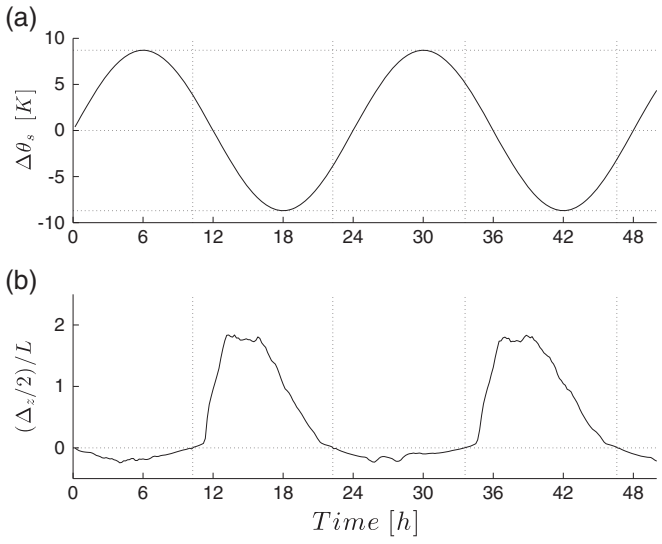

Figure 4. The figure represents the thermal forcing conditions for two *synthetic* diurnal cycles (50 h of physical time). Plot (a) shows the variation of the imposed surface temperature ($\Delta\theta_S = \theta_{s,t} - \theta_{s,t=0}$) as a sinusoidal function of time with an amplitude of 8.7 K. Plot (b) illustrates the time evolution of the atmospheric stability with z/L, being $z = \Delta z/2$. The vertical dashed lines identify the time stamps where the atmospheric stability changes (10.25, 22.25, 33.83 and 46.83 h). The horizontal dashed line identifies the change in sign.

Figure 4(a) shows the variation of the imposed surface temperature ($\Delta\theta_s = \theta_{s,t} - \theta_{s,t=0}$), and Figure 4(b) illustrates the corresponding change in atmospheric stratification, represented as z/L, with $z = \Delta z/2$ (physical height of the first numerical grid point). In both figures, the x-axis represents the 50 h of real time numerically simulated. Based on the change of sign in the stability parameter (z/L) from Figure 4(b), the simulation can be divided into five regions of alternating stability conditions, with the first region being unstably stratified. The five regions are marked with four vertical dotted lines at 10.25, 22.25, 33.83 and 46.83 h, respectively. While the manner in which the diurnal cycle is artificially enforced is not very realistic, the stratification regimes illustrate the typical diurnal scenarios. As it would be expected, large differences are encountered on the wind vector both in magnitude and in direction. Figure 5(a) shows the temporal variation of the wind turbine yaw alignment (solid line). The shaded region represents the standard deviation between the different wind turbines. It is very important to notice the difference in the standard deviation between the stably stratified regimes and the

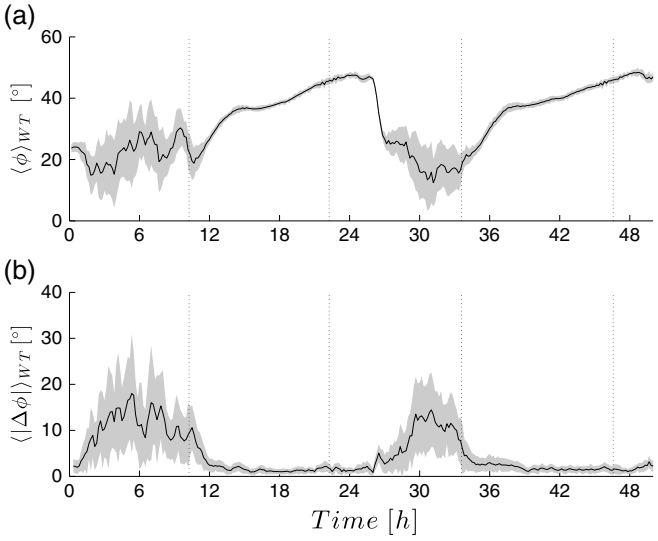

Figure 5. Temporal variation of the wind turbines' averaged yaw alignment (a), as the atmospheric stability changes (vertical dashed lines). The magnitude of correction of the WTs yaw alignment every 10 min is presented in plot (b). It better illustrates the rate of change in the turbine's yaw alignment. The shaded regions represent the corresponding standard deviations.

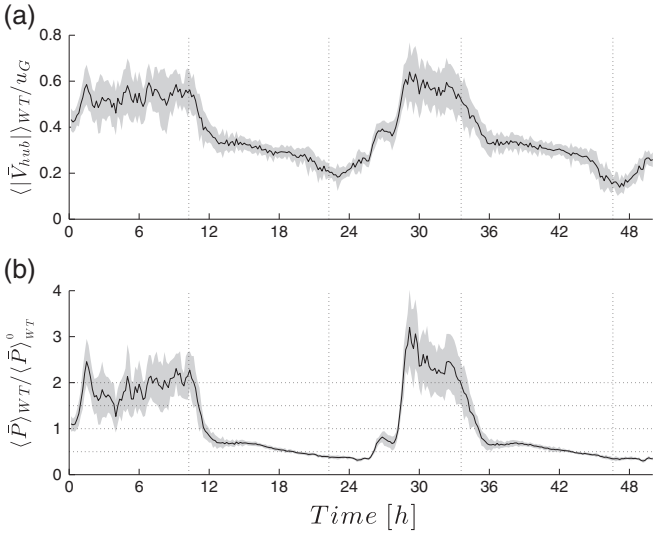

Figure 6. Time evolution of the mean velocity (a) and the extracted power (b) for the diurnal cycle study case. The shaded grey area represents the corresponding standard deviation of the mean wind velocity and extracted power between the 24 wind turbines.

DOI: 10.1002/we

unstable ones. Also note how the orientation linearly increases during the stable regimes. The rate of change in the turbine's yaw alignment is better visualized in Figure 5(b), which shows the magnitude of correction of the WTs every 10 min, averaged over the 24 WTs, together with the corresponding standard deviation. Overall, the correction in yaw during the unstable periods is an order of magnitude greater than that of the stably stratified periods. The standard deviation is also much higher during the unstable regimes as compared with the stable periods. Similar to study case (A) (Section 5), the corresponding hub height measured wind is now explored through the different stratification regimes. Figure 6(a) shows the corresponding velocity averaged over the 24 wind turbines (solid line) and the corresponding standard deviation associated with the variability between different turbines. The mean and standard deviation are greater during the unstable regimes compared with the stable periods. Correspondingly, the power extracted by the WTs from the ABL is shown with its mean and standard deviation in Figure 6(b). It is very important to realize that, contrary to the standard belief, there is much more power available during day time. However, this comes with an associated high cost given by the high spatial and temporal variance. Therefore, in order to be able to harvest the wind resources available, it is necessary that wind turbines can cope with the high temporal variability. Note that the power extracted during the diurnal cycle is normalized using the overall time-averaged power extracted from study case A (in kinematic units), shown in Figure 3(b). Because both study cases are driven by the same geostrophic forcing, this normalization provides an easy way to observe the differences in power extraction because of changes in stratification.

Further, it is interesting to look at the change in wind shear throughout the turbine's rotor disk according to the different stability regimes. During the convective periods, the flow is largely dominated by large convective plumes and enhanced turbulence intensity, thus inducing a more mixed ABL. In contrast, nights are characterized by shallower boundary layers with much less turbulence and hence a completely different velocity profile. In this case, the effect of surface roughness and enhanced drag due to the turbines is felt in a much different manner compared with the unstable stratification. At night, velocity gradients are greater, indirectly inducing a larger change of wind orientation with height. Not only is the shear enhanced during night time because of the vertical gradient of the velocity profile, but also a lateral shear is enhanced because of an increased change in wind direction throughout the rotor disk. This phenomena is well represented in Figure 7(a). Each shaded region represents a different vertical sector of the turbine's rotor disk area. It can be observed that while during the convective regimes the vertical variability of the direction of the incoming wind vector (with respect to the Cartesian x-direction) is negligible, for the stable regimes, there exists a change of even 20° throughout the turbine rotor dimensions. This enhanced vertical variability in the direction of the incoming wind vector induces a lateral shear on

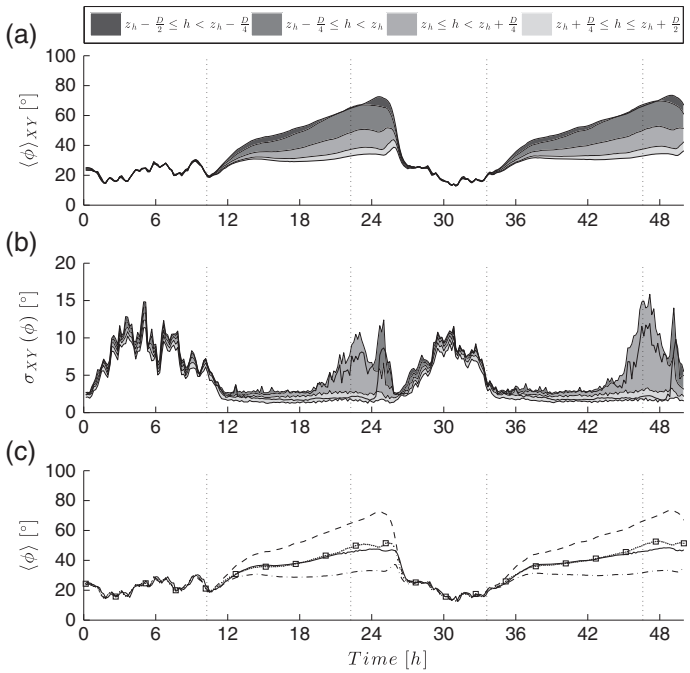

Figure 7. It shows the mean angle of the incoming wind with respect to the streamwise direction as a function of height (plots (a) and (c)). Plot (c) shows the mean angle for $z = z_h + D/2$ (dot dashed), $z = z_h - D/2$ (dashed) and $z = z_h$ (dotted with square markers) along with orientation of the wind turbines (solid) averaged over the 24 wind turbines. Plot (a) shows with a grey scale the progressive change in the angle of the mean horizontal velocity (time and planar average) as a function of height. Plot (b) illustrates the associated standard deviation.

the turbine's rotor disk. Figure 7(b) shows the associated standard deviation in the orientation of the mean horizontal velocity for the same vertical sectors as in the previous figure. It can be observed that there is larger variance during the unstable regimes; however, it can also be observed that larger vertical differences exist during the stable periods. For the sake of clarity, Figure 7(c) represents the mean wind orientation at top ($z = z_h + D/2$), bottom ($z = z_h - D/2$) and center ($z = z_h$) of the rotor disk along with the average wind turbine orientation. It is interesting to note that the wind turbine orientation follows the horizontal velocity orientation at hub height even in the stable regime in spite of the fact that the magnitude of horizontal velocity increases along the disk region, while its inclination decreases. This shows the strength of the present algorithm for wind turbines where the WTs' orientation is based on the disk-averaged velocity. Vertical variability of the angle of attack of the incoming wind vector is much more apparent from plots in Figure 7 and strongly suggests that reorienting the WTs according to a single measure taken at hub height might be far from ideal, and more advanced methods using wind Lidar technology[49] should be rapidly developed.

7. CONCLUSIONS

Until now, most LES studies related to wind energy were carried out either using a fixed pressure gradient to ensure the mean wind direction to be perpendicular to the wind turbine rotor disk or by forcing the flow with a geostrophic wind and timely readjusting the turbines orientation. In the cases studied here, it was possible to study wind farm conditions under close-to-realistic conditions with time-varying wind directions. In this work, a new LES model for a time-adaptive wind turbine has been introduced. The new algorithm enables the wind turbines to dynamically realign with the incoming wind vector. Therefore, the modelled wind turbines time adjust the yaw orientation similar to a real wind turbine. The performance of the new model was first tested under a simulation with controlled conditions. An ABL flow under neutral stratification was forced with a time-changing geostrophic wind. The dynamical yaw realignment of the wind turbines has been shown to accurately follow the orientation of the incoming wind vector. A posteriori, the new model was used to further explore the interaction between an idealized thermal ABL and an embedded wind farm. A close-to-realistic diurnal cycle was enforced with a changing surface temperature and a constant geostrophic forcing. Under these idealized ABL conditions, results show that contrary to popular understanding, there is a larger potential power to be harvested during the unstable time periods, but at the cost of designing wind turbines capable of adapting to the enhanced variance of these periods. On the contrary, stable periods provide less power but are more constant over time. Results also show that stable regimes are also characterized by an enhanced lateral shear induced by an increased change in wind direction with height. Therefore, the validity of traditional methods measuring incoming wind conditions through devices installed at the turbine's nacelle is called into question. The new LES model for time-adaptive wind turbines opens the potential for studies of a large array of real problems related to wind energy and their interaction with the surrounding atmospheric flow that previously could not be explored.

In the near future, one should consider a similar scenario with more realistic ABL forcing conditions coming from field experiments, with corresponding time-changing geostrophic forcing, to further explore the power distribution and variability through a real ABL diurnal flow. Note that the aim of the work presented was to introduce a new, more flexible, wind turbine model for being able to study more realistic ABL conditions. The two cases presented illustrate the performance of the model and show the potential use to further explore the interaction between WTs and realistic ABL flows.

ACKNOWLEDGEMENTS

The work was made possible by support received through the Swiss National Science Foundation (project no. 200021 134892/1 and 20020 125092), ETH Domain Centre for Competence in Environmental Sustainability, NSERC Discovery Grant (MBP), Swiss National Supercomputing Center (CSCS), Scientific IT and Application Support (SCITAS) group at EPFL, University of Utah and University of British Columbia.

REFERENCES

1. Snel H. Review of the present status of rotor aerodynamics. *Wind Energy* 1998; **1**(S1): 46–69, DOI: 10.1002/(SICI)1099-1824(199804)1:1+⟨46::AID-WE3⟩3.0.CO;2-9.
2. Burton T, Sharpe D, Jenkins N, Bossanyi E. *Wind Energy Handbook*. Wiley: New York, 2001.
3. Voutsinas SG, Rados KG, Zervos A. On the analysis of wake effects in wind parks. *Journal of Wind Engineering and Industrial Aerodynamics* 1990; **14**: 204–219.
4. Frandsen S. On the wind speed reduction in the center of large clusters of wind turbines. *Journal of Wind Engineering and Industrial Aerodynamics* 1992; **39**: 251–265.

5. González-Longatt F, Wall P, Terzija V. Wake effect in wind farm performance: steady-state and dynamic behavior. *Renewable Energy* 2011; **39**(1): 1–10, DOI: 10.1016/j.renene.2011.08.053.
6. Roy S, Pacala S, Walko R. Can large wind farms affect local meteorology? *Journal of Geophysical Research* 2004; **109**(D19101): 1–6.
7. Keith D, DeCarolis J, Denkenberger D, Lenschow D, Malyshev S, Pacala S, Rasch P. The influence of large-scale wind power on global climate. *Proceedings of the National Academy of Science* 2004; **101**(46): 16115–16120.
8. Kirk-Davidoff DB, Keith DW. On the climate impact of surface roughness anomalies. *Journal of Atmospheric Science* 2008; **65**: 2215–2234.
9. Barrie D, Kirk-Davidoff D. Weather response to a large wind turbine array. *Atmospheric Chemistry and Physics* 2010; **10**: 769–775.
10. Kumar V, Kleissl J, Meneveau C, Parlange MB. Large-eddy simulation of a diurnal cycle of the atmospheric boundary layer: atmospheric stability and scaling issues. *Water Resources Research* 2006; **42**: 1–18. DOI: 10.1029/2005WR004651.
11. Porté-Agel F, Wu YT, Chen CH. A numerical study of the effects of wind direction on turbine wakes and power losses in a large wind farm. *Energies* 2013; **6**(10): 5297–5313. DOI: 10.3390/en6105297.
12. Bhaganagar K, Debnath M. Implications of stably stratified atmospheric boundary layer turbulence on the near-wake structure of wind turbines. *Energies* 2014; **7**(9): 5740–5763.
13. Bhaganagar K, Debnath M. The effects of mean atmospheric forcings of the stable atmospheric boundary layer on wind turbine wake. *Journal of Renewable and Sustainable Energy* 2015; **7**(1): 013124.
14. Sescu A, Meneveau C. A control algorithm for statistically stationary large-eddy simulations of thermally stratified boundary layers. *Quarterly Journal of the Royal Meteorological Society* 2014; **140**(683): 2017–2022.
15. Gopalan H, Gundling C, Brown K, Roget B, Sitaraman J, Mirocha JD, Miller WO. A coupled mesoscale–microscale framework for wind resource estimation and farm aerodynamics. *Journal of Wind Engineering and Industrial Aerodynamics* 2014; **132**: 13–26.
16. Mirocha J, Kirkil G, Bou-Zeid E, Chow FK, Kosović B. Transition and equilibration of neutral atmospheric boundary layer flow in one-way nested large-eddy simulations using the weather research and forecasting model. *Monthly Weather Review* 2013; **141**(3): 918–940.
17. Mirocha J, Kosovic B, Aitken M, Lundquist J. Implementation of a generalized actuator disk wind turbine model into the weather research and forecasting model for large-eddy simulation applications. *Journal of Renewable and Sustainable Energy* 2014; **6**(1): 1–9.
18. Jonkman JM, Buhl Jr. ML. FAST user's guide, National Renewable Energy Laboratory, Golden, CO, *Technical Report* No. NREL/EL-500-38230, 2005.
19. Fleming P, Gebraad P, van Wingerden JW, Lee S, Churchfield M, Scholbrock A, Michalakes J, Johnson K, Moriarty P. The SOWFA super-controller: a high-fidelity tool for evaluating wind plant control approaches. *Proceedings of the European Wind Energy Association (Vienna, 2013)*, 2013.
20. Calaf M, Parlange MB, Meneveau C. Large eddy simulation of scalar transport in fully developed wind-turbine array boundary layers. *Physics of Fluids* 2011; **23**(126603): 1–16.
21. Lu H, Porté-Agel F. Large-eddy simulation of a very large wind farm in a stable atmospheric boundary layer. *Physics of Fluids* 2011; **23**(065101): 1–19.
22. Roy SB. Simulating impacts of wind farms on local hydrometeorology. *Journal of Wind Engineering and Industrial Aerodynamics* 2011; **99**: 491–498.
23. Yang X, Kang S, Sotiropoulos F. Computational study and modeling of turbine spacing effects in infinite aligned wind farms. *Physics of Fluids* 2012; **24**(11): 1–28.
24. Zhang W, Markfort CD, Porté-Agel F. Experimental study of the impact of large-scale wind farms on land-atmosphere exchanges. *Environmental Research Letters* 2013; **8**(015002): 1–8. DOI: 10.1088/1748-9326/8/1/015002.
25. Rajewski DA, Takle ES, Lundquist JK, Oncley S, Prueger JH, Horst TW, Rhodes ME, Pfeiffer R, Hatfield JL, Spoth KK, Doorenbos RK. Crop wind energy experiment (CWEX): observations of surface-layer, boundary layer, and mesoscale interactions with wind farm. *BAMS* 2013; **94**(5): 655–672. DOI: 10.1175/BAMS-D-11-00240.1.
26. Lundquist J, Bariteau L. Dissipation of turbulence in the wake of a wind turbine. *Boundary-Layer Meteorology* 2015; **154**(2): 229–241.
27. Wu YT, Porté-Agel F. Large-eddy simulation of wind-turbine wakes: evaluation of turbine parameterizations. *Boundary-Layer Meteorology* 2011; **138**: 345–366. DOI: 10.1007/s10546-010-9569-x.

28. Bou-Zeid E, Meneveau C, Parlange M. A scale-dependent Lagrangian dynamic model for large-eddy simulation of complex turbulent flows. *Physics of Fluids* 2005; **17**: 1–18.
29. Orzag SA, Pao YH. Numerical computation of turbulent shear flows. *Advances in Geophysics* 1974; **1**(224): 225–236.
30. Moeng CH. A large-eddy simulation model for the study of planetary boundary-layer turbulence. *Journal of the Atmospheric Sciences* 1984; **41**(13): 2052–2062.
31. Albertson J, Parlange M. Natural integration of scalar fluxes from complex terrain. *Water Resources Research* 1999; **23**: 239–252.
32. Albertson J, Parlange M. Surface length-scales and shear stress: implications for land-atmosphere interaction over complex terrain. *Water Resources Research* 1999; **35**: 2121–2131.
33. Canuto C, Hussaini M, Quarteroni A, Zang T. *Spectral Methods in Fluid Dynamics*. Springer-Verlag: Berlin, 1988.
34. Frigo M, Johnson S. The design and implementation of FFTW3. *Proceedings of the IEEE* 2005; **93**(2): 216–231.
35. Povitsky A, Morris PJ. A higher-order compact method in space and time based on parallel implementation of the Thomas algorithm. *Journal of Computational Physics* 2000; **161**(1): 182–203.
36. Parlange MB, Brutsaert W. Regional shear stress of broken forest from radiosonde wind profiles in the unstable surface layer. *Boundary-Layer Meteorology* 1993; **64**(4): 355–368.
37. Hultmark M, Calaf M, Parlange MB. A new wall shear stress model for atmospheric boundary layer. *Journal of the Atmospheric Sciences* 2013; **70**: 3460–3470.
38. Stull RB. *An Introduction to Boundary Layer Meteorology*. Springer: Netherlands, 1988.
39. Brutsaert W, Parlance MB. The unstable surface layer above forest: regional evaporation and heat flux. *Water Resources Research* 1992; **28**(12): 3129–3134.
40. Brutsaert W. *Hydrology: An Introduction,* (Vol. 61, No. 8). Cambridge University Press: Cambridge, 2005.
41. Brutsaert W, Parlange MB, Gash JHC. Neutral humidity profiles in the boundary layer and regional evaporation from sparse pine forest. *Annales Geophysicae* 1989; **7**: 623–630.
42. Jimenez A, Crespo A, Migoya E, Garcia J. Advances in large-eddy simulation of a wind turbine wake. *Journal of Physics: Conference Series* 2007; **75**(012041): 1–13. DOI: 10.1088/1742-6596/75/1/012041.
43. Jimenez A, Crespo A, Migoya E, Garcia J. Large-eddy simulation of spectral coherence in a wind turbine wake. *Environmental Research* 2008; **3**(015004): 1–9. DOI: doi:10.1088/1748-9326/3/1/015004.
44. Calaf M, Meyers J, Meneveau C. Large eddy simulation study of fully developed wind-turbine array boundary layers. *Physics of Fluids* 2010; **22**(015110): 1–16.
45. Meyers J, Meneveau C. Large eddy simulations of large wind-turbine arrays in the atmospheric boundary layer. *48th AIAA Aerospace Sciences Meeting Including the New Horizons Forum and Aerospace Exposition*, Vol. 827, Held at Orlando, Florida, United States, 2010; 2010.
46. Wu YT, Porté-Agel F. Simulation of turbulent flow inside and above wind farms: model validation and layout effects. *Boundary-Layer Meteorology* 2013; **146**(2): 181–205. DOI: 10.1007/s10546-012-9757-y.
47. Sorensen JN, Shen WZ. Numerical modeling of wind turbine wakes. *Journal of Fluids Engineering* 2002; **124**(2): 393–399.
48. Shepard D. A two-dimensional interpolation function for irregularly-spaced data. *Proceedings of the 1968 23rd ACM National Conference*, ACM, 1968; 517–524.
49. Mikkelsen T, Angelou N, Hansen K, Sjöholm M, Harris M, Slinger C, Hadley P, Scullion R, Ellis G, Vives G. A spinner-integrated wind lidar for enhanced wind turbine control. *Wind Energy* 2013; **16**: 625–643.